Physical Human-Bicycle Interfaces for Robotic Balance Assistance

by

Jonathan Bush

A Thesis Presented in Partial Fulfillment
of the Requirement for the Degree
Master of Science

Approved April 2020 by the
Graduate Supervisory Committee:

Wenlong Zhang, Co-Chair
Robert Heinrichs, Co-Chair
Douglas Sandy

ARIZONA STATE UNIVERSITY

May 2020

ABSTRACT

Riding a bicycle requires accurately performing several tasks, such as balancing and navigation, which may be difficult or even impossible for persons with disabilities. These difficulties may be partly alleviated by providing active balance and steering assistance to the rider. In order to provide this assistance while maintaining free maneuverability, it is necessary to measure the position of the rider on the bicycle and to understand the rider's intent. Applying autonomy to bicycles also has the potential to address some of the challenges posed by traditional automobiles, including CO_2 emissions, land use for roads and parking, pedestrian safety, high ownership cost, and difficulty traversing narrow or partially obstructed paths.

The Smart Bike research platform provides a set of sensors and actuators designed to aid in understanding human-bicycle interaction and to provide active balance control to the bicycle. The platform consists of two specially outfitted bicycles, one with force and inertial measurement sensors and the other with robotic steering and a control moment gyroscope, along with the associated software for collecting useful data and running controlled experiments. Each bicycle operates as a self-contained embedded system, which can be used for untethered field testing or can be linked to a remote user interface for real-time monitoring and configuration. Testing with both systems reveals promising capability for applications in human-bicycle interaction and robotics research.

ACKNOWLEDGEMENTS

I would express my gratitude to the members of the Robotics and Intelligent Systems (RISE) Lab at Arizona State University for the continuous interest and support for the Smart Bike project since the beginning. Special thanks to Dr. Wenlong Zhang for providing direction to the project and motivating us to apply sound engineering principles to our design. I would also like to thank Dr. Robert Heinrichs and Douglas Sandy for serving on my committee and for providing embedded systems instruction that was critical to the success of this project.

This project was also partly made possible by funding from the Master's Opportunity for Research in Engineering program offered by the Ira A. Fulton Schools of Engineering at Arizona State University. Additional thanks are extended to Rhett Sweeney, who provided invaluable guidance on design and manufacturing for this project. Furthermore, Hansol Moon's expertise in controls was critical for the development and testing of the self-balancing bicycle system.

A portion of the content in this thesis related to the force sensitive seat was continued from my Barrett Honors Thesis, which was completed simultaneously with the first year of my master's program.

TABLE OF CONTENTS

CHAPTER Page

LIST OF TABLES

LIST OF FIGURES

Chapter 1

INTRODUCTION

1.1 Background

Bicycles are a compact, affordable, and sustainable source of transportation and recreation for a large share of the world population. However, human balance impairments, such as those from stroke or Parkinson's disease, may negatively impact cycling ability. This difficulty may be partly alleviated by providing active balance and steering assistance to the rider. In addition to assistance, a robotic bicycle may also be useful for balance and motor rehabilitation, as shown by Kim *et al.* (1999) and Mohammadi-Abdar *et al.* (2015).

Over the past four decades, considerable work has gone into the creation of autonomous cars. This technology promises to provide the convenience of automotive transport without the requirements currently placed on the human driver. However, the autonomous car does not address many of the issues posed by traditional automobiles, including CO_2 emissions, increasing land use for roads and parking, pedestrian safety, high ownership cost, and difficulty traversing narrow or partially obstructed pathways (Lindsay *et al.*, 2011; Cherry, 2007). Improving the accessibility of bicycles may be an effective way to address some of these issues. Autonomous bicycles may also have applications in self-distributing rideshare systems and for delivery in urban environments.

1.2 Problem Statement

To provide balance assistance while still providing free maneuverability, it is necessary to measure the position of the rider on the bicycle and to understand the rider's intent. However, previous work in this area has largely focused on either measuring rider power output or relied on wearable sensors to obtain pose information. This leaves a gap for how to get the required information using only sensors built into the bicycle itself.

Additionally, providing balance assistance to riders requires a robotic bicycle that can act to balance itself along with a human rider. Several robotic balance bikes have been developed by research teams around the world, but these systems have been limited in both actuator capability and bicycle size. Developing a new robotic bicycle platform, overcoming these limitations, will provide an opportunity to expand the current knowledge of bicycle controls to encompass human-bicycle interaction and balance assistance.

1.3 Research Questions

This section lists the research questions that will guide the approaches taken within this thesis. The first two research questions pertain to human-bicycle interaction and the last question pertains to robotic balancing.

- How can steering intent be identified from human-bicycle interaction forces?
- How do healthy cyclists respond to induced bicycle steering disturbances?
- How can controllable balance assistance be provided in a self-contained bicycle system?

1.4 Objectives

The objectives are to first design and construct a specially instrumented bicycle for quantifying the physical human-bicycle interaction. This will consist of capturing the contact forces between the rider and the bicycle, the steering and pedal angles, the bicycle speed, and inertial measurements from the bicycle frame.

After the previously described system has been assembled, it can be used in a motion capture experiment for gathering human-bicycle interaction data simultaneously with the real-world bicycle and human motion. This data can be used to develop better models of human-bicycle interaction.

Lastly, a self-balancing bicycle robot with robotic steering and a control moment gyroscope will be developed. This system will be used for studying bicycle controls with the intent of providing balance assistance to human riders and stand-alone autonomous operation.

1.5 Scope

Two bicycles were used for this research, with one intended for human-bicycle interaction research (Bike 1) and the other for self-balancing research (Bike 2).

This thesis covers the tasks of monitoring a human rider's interaction with an instrumented bicycle and investigating how a system to balance and control a bicycle can be designed with a focus on safety, reliability, and ease of adaptation. The section on human-bicycle interaction covers the development of a force sensing system for the handlebars, pedals, and seat. The force measurements are collected and logged simultaneously with measurements from Bike 1's integrated inertial measurement unit and encoders. This system is intended to provide greater insight into human-bicycle interaction and how to effectively account for human intent when providing active assistance to a rider. Sensor selection and data acquisition are also considered.

The design and implementation of a robust robotic bicycle research platform (Bike 2) are also presented in the section on self-balancing. This section details the planning, hardware design, software development, and testing of a control moment gyroscope (CMG) and a robotic steering actuator for stationary and in-motion bicycle control. Preliminary testing to verify the system's capability is conducted in a motion-capture environment with a cascaded proportional-integral-derivative (PID) balance controller.

1.6 Limitations

Due to the COVID-19 pandemic and the subsequent limitations on product availability and shipping, the completion of the human-bicycle interaction system was severely delayed and rigorous testing with a motion capture system could not be completed. This means that it was not possible during this thesis to make any substantially new determinations about the relationship between bicycle rider pose and interaction forces. However, some outdoor testing data was collected to demonstrate the functionality of the system as described.

1.7 Outline

Chapter 2 covers previous work in the areas of human-bicycle interaction, bicycle-related health and rehabilitation, bicycle dynamics, and robotic bicycle balancing. The body of knowledge from these works serves as the foundation for the new developments in this thesis.

Chapter 3 covers the design and implementation of the human-bicycle interaction system. This includes measuring contact forces between the rider and bicycle, measuring bicycle joint angles, and measuring the motion of the bicycle frame.

Chapter 4 covers the slef-balancing system implemented with Bike 2. This system is broken down into power, robotic steering, and control moment gyroscope subsystems. The hardware and software components of each system are discussed. The capability of the slef-balancing systems is verified in a motion capture experiment with a cascaded PID balance controller.

Chapter 5 presents the results of this work, including its impact and limitations. Future work to build upon these results is also presented.

1.8 Overview of Results

For Bike 1, the development of the human-bicycle interaction system was delayed by the COVID-19 pandemic, and the planned motion capture tests could not be completed. However, all sensors were installed on the bicycle and were connected to the data acquisition system. The system's functionality was verified through a series of short outdoor tests. The sensor modules and software developed for this system provide a modular system that can be adapted for a variety of applications in subsequent robotics research, or potentially in physical therapy or sports training.

The new robotic steering subsystem and CMG developed for Bike 2 effectively meet the objective of providing steering and inertial actuation within an adaptable bicycle system. Numerous improvements to the hardware and software improved the repeatability and ease of running experiments on the bike. A cascade controller, consisting of inner and outer PID control loops, was implemented to balance the bicycle by controlling the bicycle roll angle and the CMG gimbal position simultaneously.

Chapter 2

LITERATURE REVIEW

2.1 Human-Bicycle Interaction

Previously, contact forces between a human rider and a bicycle were used by Chen *et al.* (2014) with a physical-learning model to design an extended Kalman filter for limb position estimation. This design utilized force sensors, along with inertial measurement units (IMUs) on the bicycle frame and rider trunk and encoders on the bicycle joints. This approach takes advantage of the fact that limb position is constrained by the rider trunk position and the handlebar and pedal positions. The pose estimation technique used by Chen *et al.* (2014) differs from the method proposed here by the elimination of the rider trunk IMU and the addition of more force sensors to the seat and handlebars. This approach yields the possibility of providing rider pose estimation capability without any wearable sensors. Additionally, human-bicycle interaction was studied by Kooijman *et al.* (2009), who analyzed the relationship between bicycle speed and rider motion. Stone and Hull (1993) investigated the differences in rider-bicycle interaction forces between standing and sitting riding positions.

Dozza and Fernandez (2013) developed an integrated bicycle tracking system for studying bicycle riding patterns in traffic. The system included two IMUs, GPS, cameras, and a brake pressure sensor. This configuration enabled the researchers to collect data from 19 cyclists over six months, using five similarly instrumented bicycles. The researchers searched the data for instances of hard braking, indicating potentially critical situations warranting further analysis. They also applied spectral analysis to the IMU data to characterize periodic lateral and longitudinal acceleration (Dozza and Fernandez, 2013). This work demonstrated the usefulness of field data in vehicle and driver modeling.

2.2 Health and Rehabilitation

Kim *et al.* (1999) developed a stationary bicycle training system utilizing virtual reality for postural balance rehabilitation.

The health effects of bicycling and the use of bicycles for physical training have also been studied by several groups. On a large scale, Woodcock *et al.* (2014) showed that increased use of bicycles corresponded to a decrease in mortality due to increased physical activity. Increased bicycling also resulted in a reduction in PM2.5 pollutant concentrations, which corresponded to a slight increase in respiratory health for the general population. Automated bicycles have also been used for fitness training in Leitner *et al.* (2014), where the rider's heart rate is regulated by varying the braking intensity. Integrating a system like this into a mobile platform rather than a stationary bicycle would also make the training experience more engaging. Meyer *et al.* (2015) applied sliding mode control to similarly regulate the rider's heart rate by varying the assistance supplied by an electric motor in a commercial electric bicycle. The Smart Bike system described in this thesis has the potential to provide both regulated braking and assistance.

2.3 Bicycle Dynamics

Since the invention of the bicycle in 1817, considerable work has been conducted to understand the principles behind its operation. One of the most famous early works in this area was conducted by Jones (1970), who constructed various bicycle modifications in an attempt to discern which factors of bicycle design contributed the most to self-stabilization. In his report, Jones refuted the model previously proposed by Timoshenko and Young (1948) which suggested that bicycles were balanced by the rider steering "into the direction of the fall and so travers[ing] a curved trajectory of such a radius as to generate enough centrifugal force to correct the fall" (Jones, 1970). While this theory was mathematically sound, it did not explain how a bicycle could stay balanced, at speed, without steering input from the rider.

Jones continued to disprove the theory that the gyroscopic effect of the spinning wheels, by mounting counter-rotating wheels to counteract the gyroscopic torque and observing that the bicycle can still be easily ridden. However, Jones also observes that the modified bicycle is no longer self-stable without a rider, and wrongly concludes that the gyroscopic effect accounts for riderless self-stability (Jones, 1970). Kooijman *et al.* (2009) later demonstrated, with the two-mass-skate bicycle, that self-stability is not entirely dependent on gyroscopic or caster effects.

2.4 Robotic Balancing

Automated bicycle balancing has also been demonstrated using a variety of different methods. In both Iuchi *et al.* (2005) and Keo and Yamakita (2009), steering control and variable center of gravity control with a mass balancer are demonstrated. Before that, Beznos *et al.* (1998) showed that a small bicycle could be balanced with a dual control moment gyroscope (CMG) similar to that presented by Deng *et al.* (2018). More recently Lam (2011) and Wang *et al.* (2017) have used single CMGs to balance small and large bicycles respectively. The Murata Boy self-balancing bicycle robot uses a reaction wheel to generate the stabilizing torque (Manufacturing, 2008). Previous automated balancing has either focused on balancing an autonomous bicycle without a rider, or on generating perturbations useful for studying the rider's reactions.

Chapter 3

HUMAN-BICYCLE INTERACTION

To best provide active balance assistance in a human-bicycle system, it is necessary to capture the interaction between the rider and bicycle and to understand how that interaction impacts balance control. One important distinction between stand-alone bicycle balancing and balancing with a human rider onboard is the variable center of mass. For instance, if the bicycle rider leans to the left, the center of mass or the bicycle is shifted to the left as well. Figure 3.1 shows the relationship of the center of mass for the rider, bicycle, and system, as represented by equations 3.1 through 3.4 with relation to the bicycle and rider lean angles θ_B and θ_H.

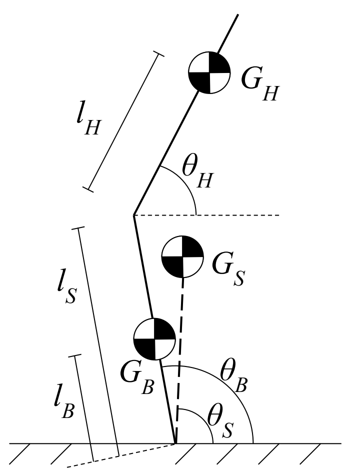

Figure 3.1: Bicycle , human (G_H), and system (G_S) centers of mass.

$$X_{Gs} = \frac{M_B l_B \cos(\theta_B) + M_H \big(l_H \cos(\theta_H) + l_P \cos(\theta_B)\big)}{M_B + M_H} \tag{3.1}$$

$$Y_{Gs} = \frac{M_B l_B \sin(\theta_B) + M_H \big(l_H \sin(\theta_H) + l_P \sin(\theta_B)\big)}{M_B + M_H} \tag{3.2}$$

$$\theta_S = \arctan 2(Y_{Gs}, X_{Gs}) \tag{3.3}$$

$$\theta_{target} = \theta_B - \theta_S + \frac{\pi}{2} \tag{3.4}$$

Quantifying the interaction between a human rider and a bicycle requires knowledge of the bicycle state and the forces applied at contact points between the rider and the bicycle, shown in Figure 3.2. The bicycle state is defined by the bicycle's orientation, velocity, and joint angles. These measurements are respectively obtained through the use of an IMU, Hall effect sensors, and rotary encoders. Interaction forces are measured by load cells installed between the human contact areas and the bicycle.

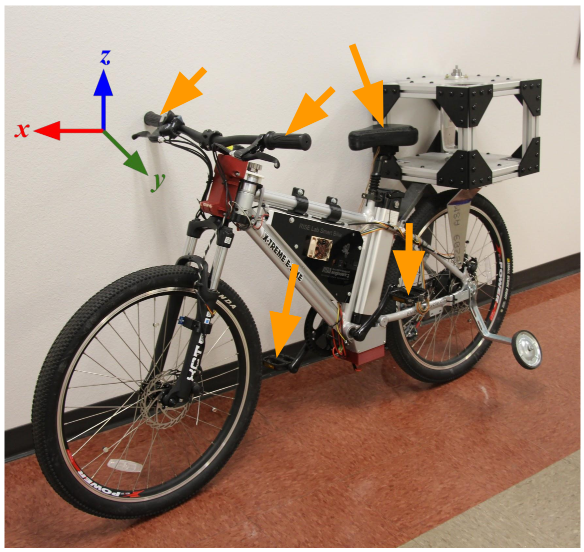

Figure 3.2: Human-bicycle interaction force locations.

3.1 Hardware

The sensor system developed in this chapter is intended to be minimally invasive and does not require the rider to attach any sensors to their body or to make any special accommodations for the sensors on the bike. However, several necessary modifications were made to the bicycle to support the addition of force sensing elements. These include replacement of the original bicycle seat with the force-sensitive bicycle seat, replacement of the handle grips with custom handle grips attached to the F3G load cells, and attaching the FCB load cells to the bicycle pedals. Rotary encoders are employed to measure the bicycle crank angle and the steering angle. Figure 3.3 shows the human-bicycle interaction related components of Bike 1.

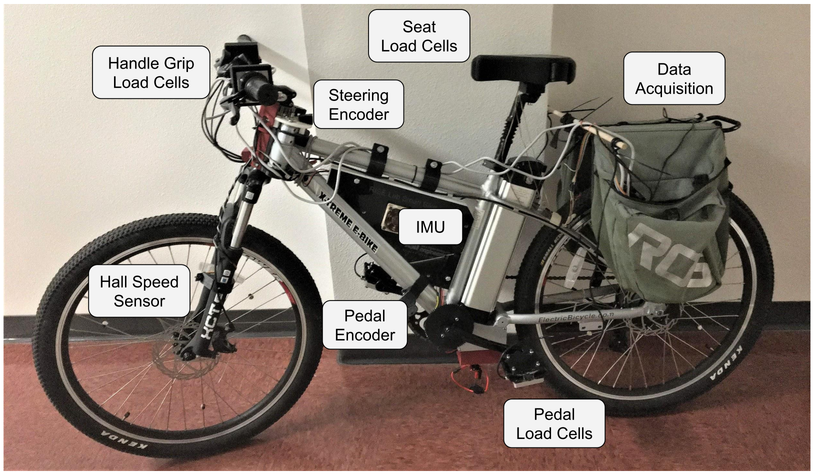

Figure 3.3: Major components of the human-bicycle interaction measurement system.

3.1.1 Seat

The force-sensitive bicycle seat is used to measure the vertical forces applied to the seat by the rider. The seat incorporates three button load cells oriented in a triangular pattern so that the center-of-pressure can be calculated from the three force measurements. Center-of-pressure on a bicycle seat was shown to be related to rider pose by Bressel and Cronin (2005), who collected seat pressure distribution using a mat of force sensors layered onto the surface of the bicycle seat. Their work showed that a forward riding position resulted in the center of pressure shifting toward the anterior (front) region of the seat relative to an upright riding position (Bressel and Cronin, 2005).

Three FX1901 (TE Connectivity, Schaffhausen) button load cells are used for measuring seat force and center of pressure. These sensors were selected due to their small size and full-scale range of 1 kN. The small size enables the sensors to be installed underneath the bicycle seat without interfering with the rider's legs. The sensors have a rated output response of 20 mV/V, which is easily measurable with the ADC in the microcontroller. The sensors are arranged equally along a three-inch radius circle underneath the bicycle seat. The sensors are aligned so that they measure forces applied to the front, back right, and back left portions of the seat. The bicycle seat is attached to a pressure plate that distributes the seat load to the three load cells in the bottom sensor fixture. The sensor fixture is securely mounted to the top of the bicycle seat post. The load cells are oriented so that one sensor is aligned with the X-axis of the bicycle, and the other two sensors form a line parallel to the Y-axis of the bicycle under the rear of the seat. This configuration allows the force vectors in both axes to be measured (Bush, 2019). Figure 3.4 shows the assembled seat installed on Bike 1.

Figure 3.4: Force-sensitive bicycle seat.

3.1.2 Handlebars

The handlebars are the second contact point between a bicycle rider and the bicycle. The rider applies forces to both handle grips to support themselves and to steer the front bicycle fork. To get the most useful information out of handlebar force measurements, two three-axis load cells were chosen to capture the full force vector applied to each handle grip. The bicycle handle grip is installed over a special mounting rod, which coupes the handle grip to one side of the load cell. The other side of the load cell is coupled to the handlebar with a connector, as shown in Figure 3.5 with the sensor shroud removed. The mount (right) bolts onto the handlebar and holds the 3-axis load cell (center) in place so that the forces applied to the handle grip (left) can be measured.

Figure 3.5: Force sensing handle grip.

The handlebar force measurement system also includes a rotary encoder to measure the angular position of the front fork relative to the bicycle frame. This is important because the direction of the force vector relative to the handlebar changes as the handlebar is rotated. Measuring the angular position of the front fork allows the force vectors measured in the handlebar frame to be transformed back to the bicycle frame. The bicycle trajectory is also dependent on the steering angle, so recording the steering angle is critical for further analysis of bicycle motion.

Three-axis force transducers were benchmarked and selected based on the following criteria: range, price, size. The first sensor benchmarked was the FNZ-100N (Forsentek, Shenzhen) 3-axis force transducer, which has a measurement range of ±100 N. The main advantages of this sensor are its small size and low cost. However, the low measurement range necessitates the use of at least two sensors on each handle, which greatly increases the design complexity of the system. Using a larger sensor with a greater measurement range and the ability to measure forces in two or more directions simplifies the design by allowing the use of only one force transducer for each handle.

The next sensor benchmarked was the TR3D-B-250 (Michigan Scientific, Charlevoix), with a measurement range of $\pm$250 lbf (1.1 kN). The primary advantages of this sensor are its small size and high measurement range. Due to these advantages, one sensor would be sufficient to measure the forces applied to a handle grip. However, the sensor has a high cost and a low maximum moment capacity of 16 Nm. This means that the sensor calibration could be degraded if a larger torque is applied to the sensor, which is likely in this application.

Finally, the F3G-1kN (Forsentek, Shenzhen) multi-axis load cell, which has a measurement range of 1 kN and a maximum excitation of 15 V, was benchmarked. With this configuration, it is possible to obtain a response of 0.015 mV/N, which can be measured directly with the Delta-Sigma analog-to-digital converter in the microcontroller. The cost of this sensor is also less than half that of the TR3D-B-250 and the large sensor range ensures that the sensor will not be saturated of the rider applies a large force. This sensor was selected for the final design.

3.1.3 Pedals

Measuring forces applied to the pedals is one of the more difficult and important tasks required to capture a full picture of the human-bicycle interaction. Several approaches exist for measuring bicycle pedal forces. One approach is to measure the net torque applied at the bicycle crankshaft or rear hub, which is a common technique in bicycle power meters (Cline, 1991). It is possible to approximate the pedal force by dividing the torque by the crank length (and gear ratio if using a rear hub torque measurement). Adding an encoder to track the crank position, as shown in Figure 3.6, further improves the force estimation, as torque is defined by the cross product of the pedal force vector and the crank arm vector. The pedal encoder is coupled to the crankshaft with the large gear, which is split into halves for easy installation. If the pedal is assumed to be flat throughout the cycle (thus the force vector is directed straight downward), a force estimation can be made with 3.5, where τ is the torque, L is the crank length, and θ is the pedal angle.

$$F = \frac{\tau}{L \cos \theta} \tag{3.5}$$

To obtain an even better approximation of pedal force using a torque sensor, it is necessary to account for the pedal angle as well. This requires installing an additional encoder to measure the angle of the pedal relative to the crank, as done by Álvarez and Vinyolas (1996) in the form of a potentiometer.

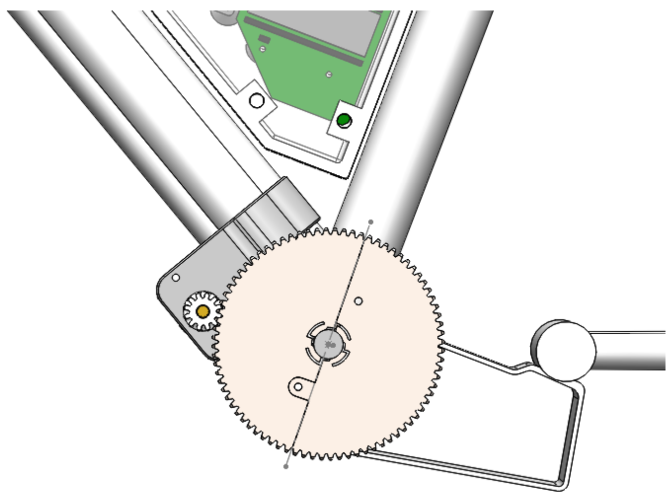

Figure 3.6: Pedal encoder assembly.

An alternate approach to obtaining pedal force measurements is to include a force sensor directly in or on the bicycle pedal. This approach is the most accurate because the need to measure two additional parameters (pedal and crank angle) is eliminated. This approach is adopted here.

The FCB-B (Forsentek, Shenzhen) pedal load cell was selected for measuring pedal interaction forces. The FCB-B has a range of 1 kN and a rated output response of

1.5 mV/V. Before the selection of this force sensor, several alternative sensors were investigated. These include a force-sensitive resistor (FSR) grid layered on the top of the pedal, and a custom force plate using the FX1901 load cell. The FSR grid was not suitable for this application because it cannot provide accurate measurements when force is applied to more than one resistor in the grid. Since the rider's shoe distributes the force across a large area, the force sensor must be capable of measuring the total force accurately. The FX1901 solution was not used because it required manufacturing multiple components to reproduce the functionality of the FCB-B, which already has the correct form factor and specifications for this application.

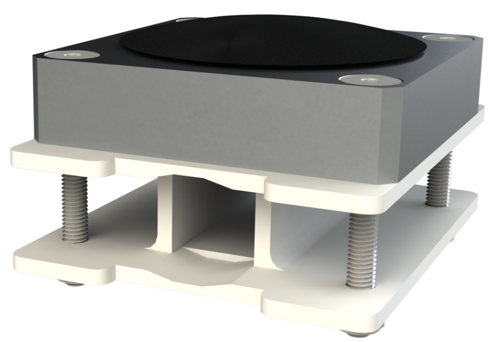

Figure 3.7: Pedal load cell.

The sensor is connected to a mounting plate that clamps around the bicycle pedal, as shown in Figure 3.7. The main disadvantage of mounting load cells on the bicycle pedals is the need to route the sensor cable so that it does not become caught in the rotating cranks. The sensor cables are attached to a pole behind the seat, which holds the cables away from the chain and cranks, so that they do not get caught or tangled. This configuration is shown in Figure 3.3, which shows the major components of Bike 1. With this configuration, it was possible to conduct several experiments without any issues with cable entanglement.

3.1.4 Bicycle Motion

To gain a full understanding of the interaction between the rider and bicycle at a given instant, it is also necessary to have some knowledge of the bicycle's motion. The system also contains several sensors to determine the orientation and velocity of the bicycle itself. These include an IMU and Hall effect sensors. The IMU measures linear acceleration, angular velocity, and magnetic field orientation, and fuses these measurements to estimate the absolute orientation of the bicycle frame. The IMU used for this purpose is a PhidegetSpatial 1044 (Phidgets, Calgary), which connects to the data acquisition computer over USB. The IMU is capable of providing absolute orientation data at up to 250 Hz with the built-in sensor fusion mode.

Measuring the speed of the bicycle is accomplished with Hall effect sensors mounted to the bicycle forks. Magnets attached to the wheel spokes trigger the Hall effect sensor when they come within close proximity. Each wheel has three magnets installed equidistantly on the spokes. When a magnet passes the Hall effect sensor, an interrupt service routine records the time since the last trigger and resets the timer. By measuring the time between sensor triggers, the angular velocity of the wheel can be determined. Multiplying the angular velocity of the wheel by the wheel radius yields the bicycle velocity.

The inclusion of separate speed measurements for each wheel is intended to provide the capability for investigating differences in wheel slip and travel distance between the front and rear wheels.

3.2 Software and Data Acquisition

The load cells described in the previous sections utilize strain gauges to measure the deformation in the sensor material as forces are applied. A strain gauge works by changing the length of a resistive element applied across the deforming material. The strain gauge is connected inside a Wheatstone bridge configuration that produces small output voltage changes corresponding to the change in resistance across the strain gauge. This output voltage can be measured and used to determine how much force is being applied, based on the material characteristics.

Load cell sensitivity is measured in mV/V, indicating the output voltage at full capacity over the excitation voltage. For instance, if a sensor (such as the F3G-1kN) has a sensitivity of 1 mV/V, a capacity of 1 kN, and a 10 V excitation, the output voltage per newton would be 0.01 mV/N. Measuring this output requires a high sensitivity data acquisition system.

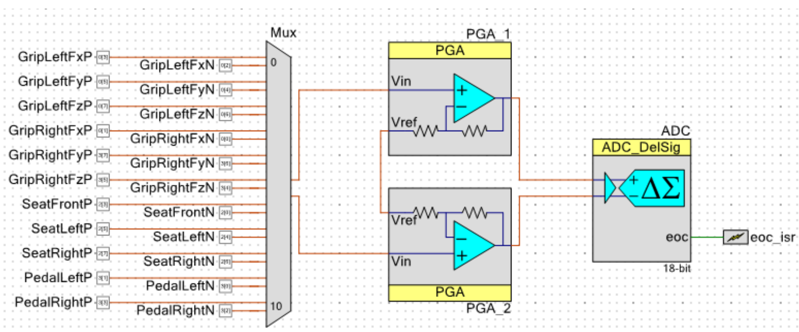

Figure 3.8: Load cell data acquisition circuit.

As shown in Figure 3.8, an analog differential multiplexer is used to select an analog signal pair from one load cell to feed into the differential amplifier and analog to digital converter (ADC). In this case, a Delta-Sigma ADC is used to obtain a high precision measurement from the ADC with a preamplification gain of 16 V/V. The advantage of using a Delta-Sigma ADC over a successive approximation register (SAR) ADC comes down to its precision. This kind of ADC works by producing a bitstream where the ratio of high to low bits corresponds to the magnitude of the analog input signal. The bitstream is fed into a digital filter, which averages the digital signal over time. The simplicity of the Delta-Sigma modulator enables the ADC to take many samples in a short amount of time, reducing the quantization error inherent in methods that use fewer samples per conversion.

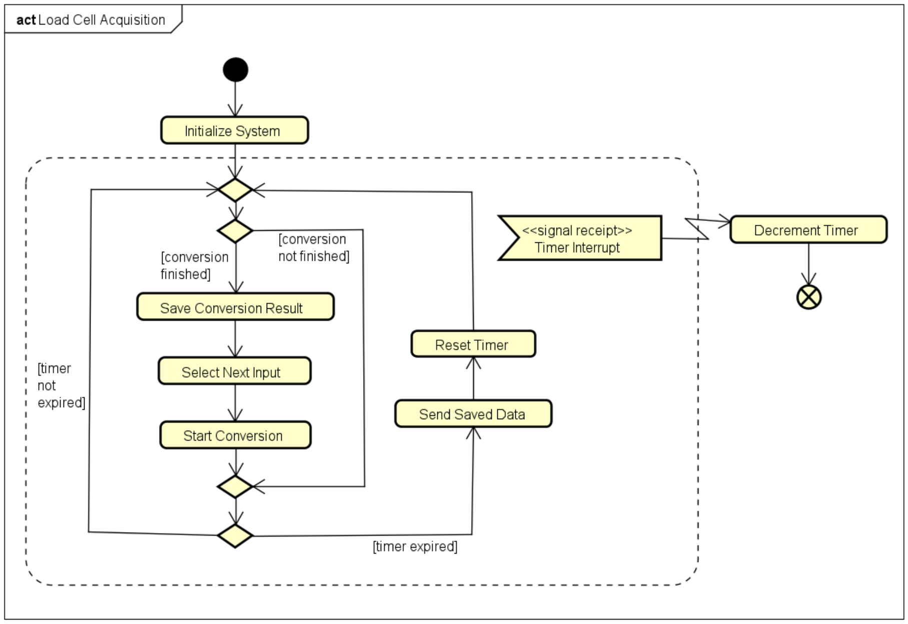

Figure 3.9: Data acquisition system activity diagram.

The flow of execution for the data acquisition system in the microcontroller is shown in 3.9. In this process, the system is initialized at startup and executes a continuous loop acquiring new ADC conversion results for each multiplexer input and saving them in an internal buffer. When the timer triggers a logging event, the saved data are sent to the connected PC and the timer is reset. The advantage of this structure is that data capture can be performed at a precise frequency, independent of the ADC sampling rate, which enables easier synchronization with data collected from a motion-capture system.

The operator can also zero the system by pressing a button on the microcontroller. This triggers the microcontroller to take the average of 1000 samples from each sensor, which is then subtracted off from following measurements before the data is transmitted to the PC. This is required to compensate for natural sensor offsets and the force applied to components by gravity.

Each load cell is supplied with a regulated 5 VDC excitation, an amplifier gain of 16 V/V, and 18 bit ADC width. The scaling factor s for conversion between the raw ADC conversion result (after subtracting the sensor offset) and the force value is shown in equation 3.6. r_{adc} is the positive ADC input range in volts, b is the number of bits in the ADC conversion result, r_{sensor} is the positive force range for the load cell, m_{sensor} is the load cell response in V/V, e is the excitation in V, and g is the amplifier gain.

$$s = \frac{r_{adc}}{2^{b-1}} \cdot \frac{r_{sensor}}{m_{sensor}} \cdot \frac{1}{e \cdot g} \tag{3.6}$$

The sensor readings are sent as unscaled 32-bit signed integers, where the scaling factors are applied for real-time graphing or the raw data is logged for further analysis.

3.3 System Testing

3.3.1 Setup

The functionality of the human-bicycle interaction measurement system was verified by conducting several trials riding the bike along a pre-planned path in the flat parking lot outside of the laboratory building. For the 10-second test segment shown in Figure 3.10, the bicycle was being ridden in a straight line at a constant velocity of 4.5 m/s. The force signs correspond with the axes shown in Figure 3.2.

Further motion-capture testing is required to collect the data required for making pose predictions from force data. The motion-capture tests would consist of several trials riding a bicycle along a pre-planned route in different riding positions. The motion-capture data and force data could be synchronized and used to train a neural network to predict the human joint positions based on the bicycle forces and motion.

Due to the COVID-19 pandemic, these tests could not be conducted during the completion of this thesis.

3.3.2 Results

The plot clearly shows the periodic shifting of forces between the left and right sides of the bicycle, corresponding with the cycling pedaling motion. An interesting phenomenon is the rider pulls back and upward on the handlebars with both hands on every pedal stroke. However, the rider applies a greater force on the side of the active pedal stroke. For instance, if the rider is applying pedal force with the left foot, the rider will apply greater handlebar force with the left hand, as seen at t=49s. It can also be seen that weight distribution shifts between the left and right sides of the bicycle seat with the pedal cycle, with more weight being supported by the side of the seat corresponding to the active pedal stroke side.

3.3.3 Potential Improvements

Several areas for potential improvement were identified while conducting the tests. These changes would improve the ease of conducting tests and the accuracy of the data collected.

The first area for improvement is the configuration and placement of the pedal load cells. The selected FCB-B load cells have a domed metal force plate on the top, which transmits the applied force to the internal load cell. This design is compact and robust. However, the dome shape of the force plate makes it difficult for the subject to keep their foot on the bicycle pedal. If the domed plate were replaced with a flat plate, this issue would be eliminated. Another problem is that the force sensor adds weight to the top of the pedal, causing the pedal to rotate so that the force sensor is on the bottom. The pedal must be rotated when mounting the bicycle. This issue could

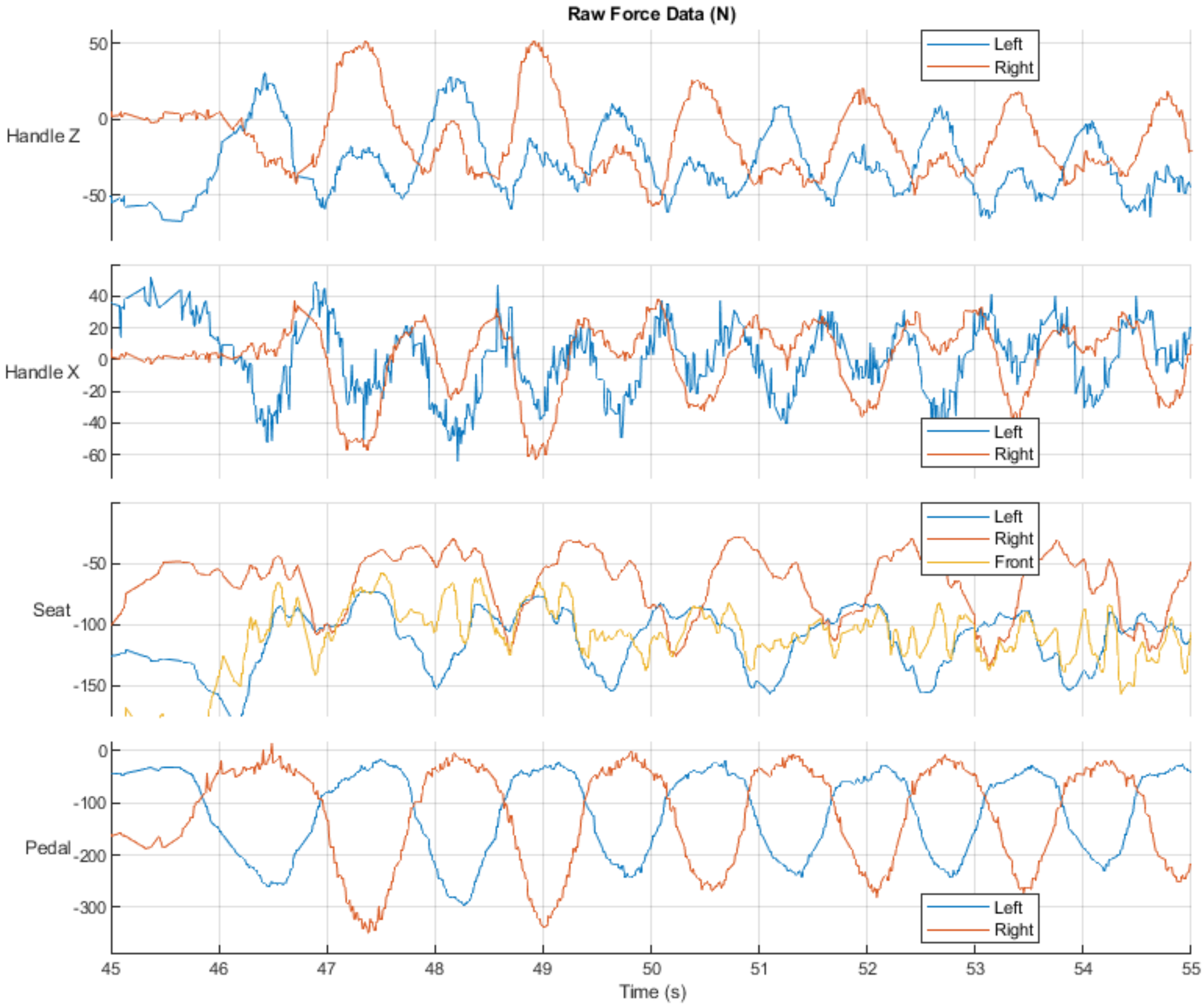

Figure 3.10: Force data collected while riding the bicycle in a straight line at constant velocity.

be remedied by adding a counterweight to the bottom of the pedal, or by replacing the pedal with a mounting fixture. The proposed mounting fixture would allow the pedal load cell to be mounted inline with the pedal axis so that the pedal would stay upright when the foot is removed.

The second area for improvement is the button load cells used for the force-sensitive bicycle seat. Each load cell has a rated range of 445 N (100 lbf), and there are three load cells. While this means that the seat has a maximum capacity of 1335 N (300 lbf) if the load is distributed equally among the three load cells, a single load cell can be saturated if more than 445 N is applied to that region of the seat. This could be remedied by replacing the FX1901-0100 load cells with the FX1901-0200 model. This replacement has the same form factor, and could thus be directly substituted by only changing the response parameters in the data acquisition system. This substitution was not previously performed due to the FX1901-0200 being temporarily out of stock. The seat load cell responses should also be properly characterized with a universal testing machine (UTM) or with calibration weights.

Chapter 4

SELF-BALANCING

The Bike 2 system consists of several major subsystems as shown in Figure 4.1, including a control moment gyroscope (CMG), steering actuator, and hub motor, which enable the bicycle's motion to be controlled. The primary objective of this section is to relate the development of a new CMG control system for stationary bicycle balancing. A CMG can create non-anchored torque in the system, enabling stationary balancing. The steering control system allows the angular position of the bicycle front fork to be controlled so that the bike can be steered while in motion. Constant velocity balancing of the Smart Bicycle was previously demonstrated in Deng *et al.* (2018).

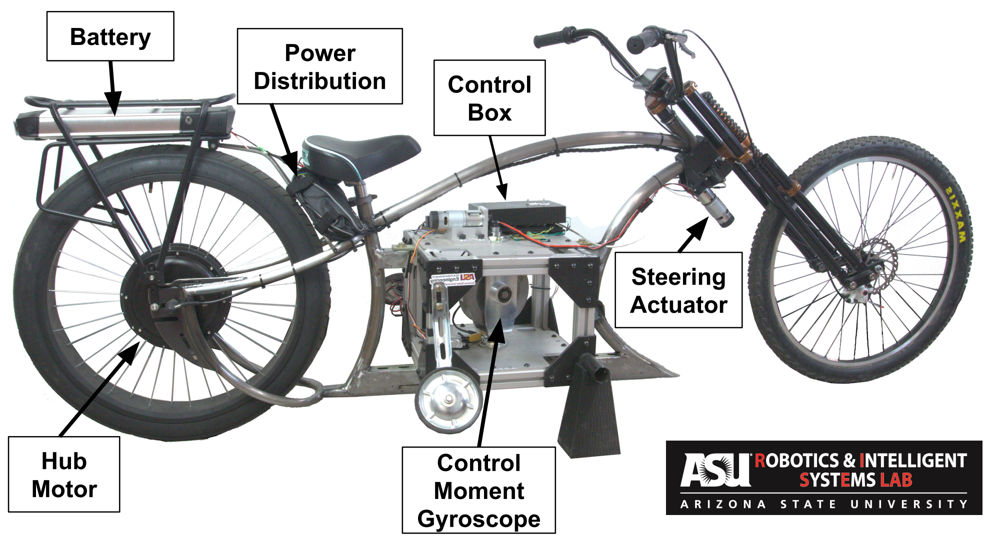

Figure 4.1: Smart Bike 2 major components.

A complete computer-aided design (CAD) model was also constructed to obtain accurate geometric and mass parameters of the bicycle system. The CAD model is shown in Figure 4.2 and the mass properties in table 4.1. The origin is the contact point between the rear tire and the ground.

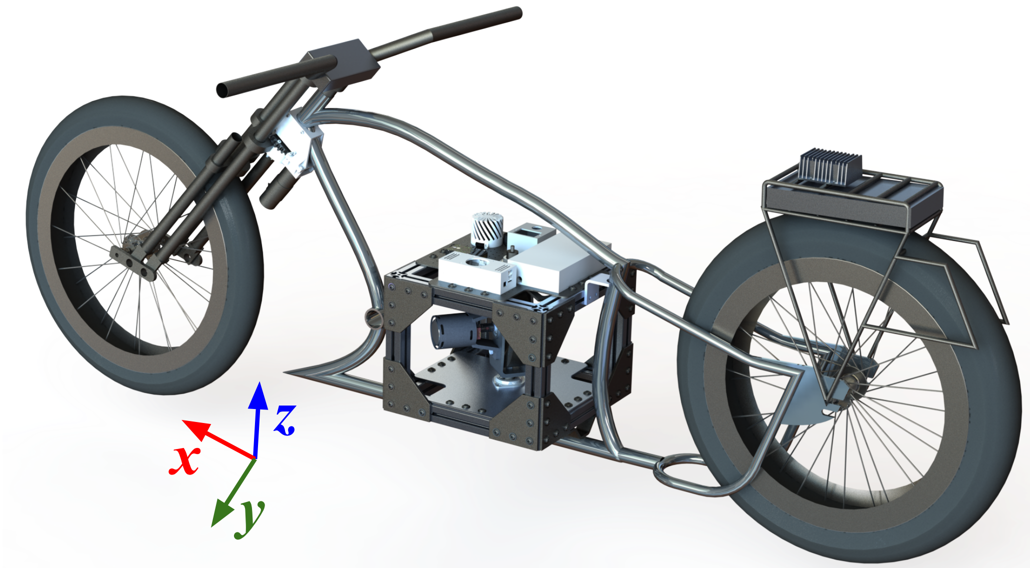

Figure 4.2: Smart Bike 2 CAD model.

X	Y	Z	m
0.72 m	0.00 m	0.46 m	73.8 kg

Table 4.1: Center of mass coordinate and bicycle mass for Bike 2.

The self-balancing system implemented on Bike 2 consists of two major subsystems: a robotic steering actuator and a CMG. The two subsystems are designed to work closely together to provide both balance and trajectory control for the bicycle. Both subsystems are linked to the same microcontroller which handles low-level balance control and provides an interface for motion control from a high-level computer, such as the Nvidia Jetson.

The microcontroller used in this implementation is a 32-bit Arm Cortex-M3 PSoC 5LP from Cypress Semiconductor. The main advantage of this chip over conventional MCUs is its greater adaptability from the addition of user-configurable analog and digital blocks. This feature enables the elimination of many external components and can also offload many resource-intensive processes from the CPU. The Bike 2 electrical system is represented in Figure 4.3, which shows the interconnections between system components.

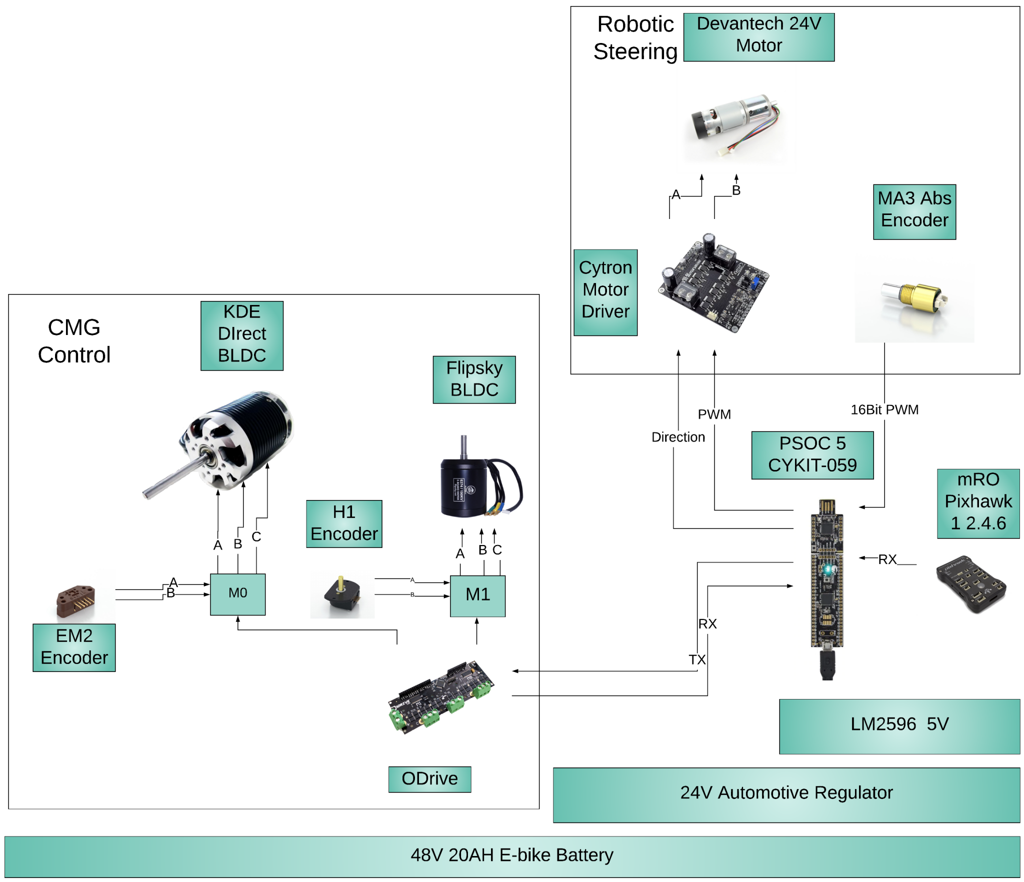

Figure 4.3: Electrical block diagram.

4.1 Power

The power subsystem of Bike 2 distributes electrical energy from the bicycle's internal battery to all onboard electronic subsystems. The power subsystem is divided into three voltage rails, which supply power for different applications within the bicycle. The electrical system provides an unregulated 48V DC rail for high power applications, such as the CMG motors. The 48V rail is powered from the bicycle battery and is protected by a 30A fuse and an emergency stop button, which triggers a relay to disconnect all power when pressed. A regulated 24V DC rail for intermediate power applications, such as robotic steering and high-level computing, is derived from the 48V rail with a step-down voltage regulator that can supply up to 20A. The voltage is further reduced to a 5V DC rail for microelectronics, such as the central microcontroller, IMU, and any USB peripherals.

4.2 Robotic Steering

Steering control is the primary method used for bicycle balancing while the bicycle is in motion. Robotic steering balances the bicycle while it is rolling forward by steering toward the lean direction of the bicycle. When the bicycle steers into the lean, this causes the base of the bicycle to move toward the center of mass of the system. By keeping the center of mass over the wheel contact points, the bicycle will remain upright. The amount of steering action depends both on the lean angle to be corrected and on the bicycle speed, as shown by Jones (1970). If the bicycle is moving faster, the required steering action is less as the greater speed will result in faster lateral motion during steering.

Controlling the bicycle steering is also essential for automated navigation, which is a future goal for the Smart Bike project. The main drawback of steering control is its inability to balance the bicycle by itself at low speeds, which is primarily addressed by the control moment gyroscope presented in section 4.3. For stationary balancing, steering control can be used to supplement the CMG through the addition of an additional cascade control loop to the stationary balance controller. This cascade control loop controls the angular velocity of the bicycle steering assembly to generate a torque counteracting the torque due to gravity. The controller also drives the steering actuator to re-center the handlebars to prevent actuator saturation.

An improved version of the robotic steering system initially developed in Deng *et al.* (2018) was implemented for the new Smart Bike 2 platform. The robotic steering system enables automated balance and trajectory control while the bicycle is moving forward. This system consists of the steering control actuator, shown in Figure 4.4, and the previously described microcontroller and inertial measurement unit. This system can operate as a closed-loop servo for steering angle, or as an open-loop torque actuator.

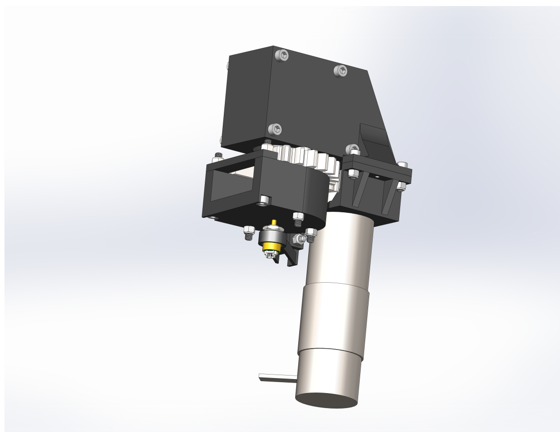

Figure 4.4: The robotic steering actuator acts as a servo to control the steering fork angle.

The steering actuator consists of a DC motor, a motor driver, an absolute magnetic encoder, and a gearbox to couple the motor to the front fork. The steering actuator is designed to be affixed to the bicycle without any mechanical modifications to the frame. This is achieved by clamping the steering gear to the bottom of the triple-tree fork steering tube and clamping the motor mount around the bicycle frame. The absolute rotary shaft encoder is inserted into the center of the steering gear assembly and is held in place relative to the bicycle frame. Having the encoder connected directly to the front fork eliminates error from gear backlash that was present in the previous design. Using an absolute encoder eliminates the requirement of initializing the zero position each time the bicycle is powered up. The 12-bit magnetic encoder yields an angular resolution of 0.088 degrees.

An EMG49 gearmotor, with an integrated 49:1 planetary gearbox, is used for the steering actuator. In combination with the external gear train, the actuator has a total gear ratio of 98:1, which yields a maximum output torque of 20 N-m. The motor is mounted underneath the bicycle frame bottom tube so that the steering motion is not obstructed by the motor. When the motor is turned off the bicycle can still be steered normally by a rider, with minimal resistance.

The steering position is maintained by a PID control loop running on the microcontroller, which activates the steering motor to minimize the error between the absolute encoder reading and the steering setpoint. Safety is improved by utilizing a second rotary attached to the motor shaft to detect motor slipping. If the motor is spinning but the front fork is not turning correspondingly, the motor is automatically disengaged to prevent any further damage.

The steering actuator can also be operated in open-loop velocity control for stationary balancing, where the wheel is rocked back and forth to shift the bicycle center of mass. It may also be possible to implement an autonomous track stand, where the wheel is turned to the side and the rear hub motor is used to rock the bicycle back-and-forth to maintain balance.

4.3 Control Moment Gyroscope

The Smart Bike's CMG is intended to provide an internally-generated torque to balance the bicycle while stationary. This torque comes from a change in the direction of the angular momentum of the spinning flywheel. The CMG used for Bike 2 is the result of several iterations of hardware and software improvement. The CMG operates as a self-contained unit within the bicycle frame. The CMG unit need only be connected to a power source - the bicycle's internal battery in this case - to provide the capacity of bicycle balance control.

4.3.1 Hardware

Substantial hardware improvements to the CMG were made during the transition from Bike 1 to Bike 2. The initial dual-CMG design featured in Deng *et al.* (2018) was abandoned after several design flaws were found with respect to the motor selection and gimbal spacing. After constructing a more accurate mathematical model for a single CMG, it was determined that lowering the CMG closer to the ground would also lower the bicycle's center of mass. Having a lower center of mass reduces the amount of torque required to keep the bike upright, as the torque due to gravity is lessened proportionally. A new bicycle frame, long enough to mount the CMG underneath the top tube between the wheels, was procured and modified to accept the CMG module.

The second CMG iteration included a brushless DC (BLDC) motor to drive the flywheel and a brushed DC motor to drive the gimbal. Position feedback for the gimbal was obtained from a rotary optical encoder mounted on the bottom CMG shaft underneath the CMG box. The flywheel motor was driven by a heavy-lift UAV electronic speed controller (ESC) from KDE Direct. The gimbal motor was driven by a Cytron DC motor controller by controlling the duty cycle and polarity of the motor power. Both motor drivers were controlled by PWM signals from the bike microcontroller. The gimbal motor, with a 49:1 planetary reduction gearbox, was able to generate enough torque to meet the CMG criterion; however, the gearbox introduced approximately 5°of backlash and slow spool-up time. Sensorless operation of the BLDC motor driver also led to difficulty with flywheel spool-up, often leading to over-current conditions and requiring manual starting of the flywheel.

The weaknesses of the second CMG iteration were addressed in the following redesign, where the KDE direct ESC was replaced with an ODrive Robotics high-performance BLDC motor driver. The ODrive is capable of simultaneously driving two motors with up to 120 A at 56 V. The ODrive also utilizes position feedback from a rotary encoder to synchronize the power phase with the motor pole positions. This sensor-based motor control allows the motors to be started smoothly from rest and to be controlled precisely. The ODrive also provides closed-loop position and velocity control, and can be commanded through a standard UART interface.

4.3.2 Software

Low-level balance control using the CMG is implemented on the primary micro-controller that is also utilized for robotic steering. A timer interrupt driven control loop structure is implemented to provide consistent execution timing for the realtime balance controller while also allowing for asynchronous processing of incoming messages. The components shown in Figure 4.5 define the interface between the controller code and the external electronics.

The software is designed with testing in mind, and provides capabilities for both remote operation and manual triggering with a button on the bicycle. This setup makes it possible to perform controlled and repeatable experiments while maintaining safety.

An easy to use user interface was developed for controlling bicycle experiments from a connected PC. This interface, shown in Figure 4.6, allows the operator to set control gains without the need to reprogram the microcontroller. The addition of this capability to Bike 2 greatly expedited the testing process, since many iterations can be executed quickly without requiring the full startup sequence to be executed each time.

Each configurable property within the bicycle controller is identified by a unique

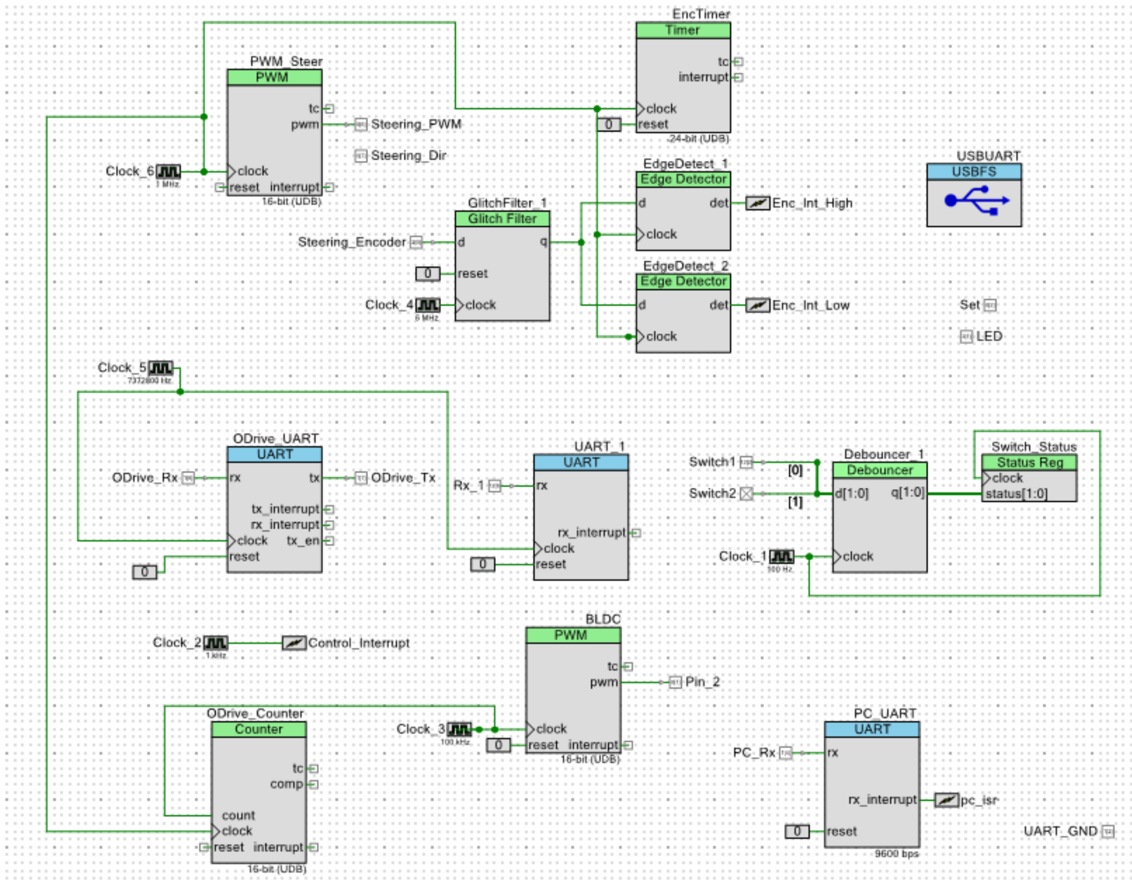

Figure 4.5: Components within the PSoC configuration for Bike 2

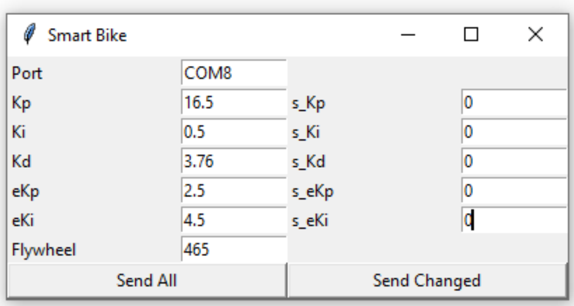

Figure 4.6: User interface for configuring control gains at runtime.

ID and can be modified by sending a message to the microcontroller with the ID and corresponding new value. If the ID in the message matches an ID in the system, the value of that property is overwritten with the new value. To avoid data corruption, the change is processed within an interrupt service routine while the execution of the main control loop is briefly paused.

To maintain consistent timing for each of the independently operating control loops, a timer-driven scheduling system is implemented to trigger events based on their associated periods. Every millisecond, a timer interrupt decrements the timer counter for each controller. When the timer expires, the controller function is called and the controller period is added to its timer. Adding the period to the timer instead of resetting the timer to the period value ensures that the average execution time will remain consistent with the period over time.

When the system is first powered on, the controller waits for the start button to be pressed. Pressing the button starts the initialization procedure, where the microcontroller verifies that all sensors on the bike are functional and runs the motor calibration procedure. During the motor calibration process, the ODrive slowly rotates the gimbal and flywheel motors to determine the alignment of the motor poles with the encoder discs. This calibration enables smooth velocity control of the motors, which is essential for the balance controller.

After the initialization process has successfully completed, the controller again waits for the operator to start the flywheel spinup process. During the flywheel spinup process, the ODrive operates the flywheel motor under current control. Current control mode applies a constant current to the motor, providing a smooth spin up to the target velocity without overloading the battery. Once the measured flywheel velocity reaches the target velocity the ODrive is switched to velocity control mode, which maintains a precise angular velocity with a PID controller.

Next, the operator triggers the microcontroller to transition to balance control mode. Initially, the control gains are set very low so that the gimbal will not respond unpredictably when the operator is not prepared. The operator sets the desired control gains using the previously described user interface, shown in Figure 4.6. In balance the control mode, the bicycle continuously sends data back to the connected PC for logging, which can be synchronized with motion capture data for further analysis.

The control software is divided into several files, which provide the core functionality of the balance controller and interfaces to external hardware, as shown in Figure 4.7. The main file contains the initialization steps for the system and the cascaded PID balance controller implementation, as described in Figure 4.4. APIs were developed for the ODrive Robotics motor controller and the robotic steering system. The Mavlink library was ported to the PSoC platform for interfacing with the Pixhawk flight controller.

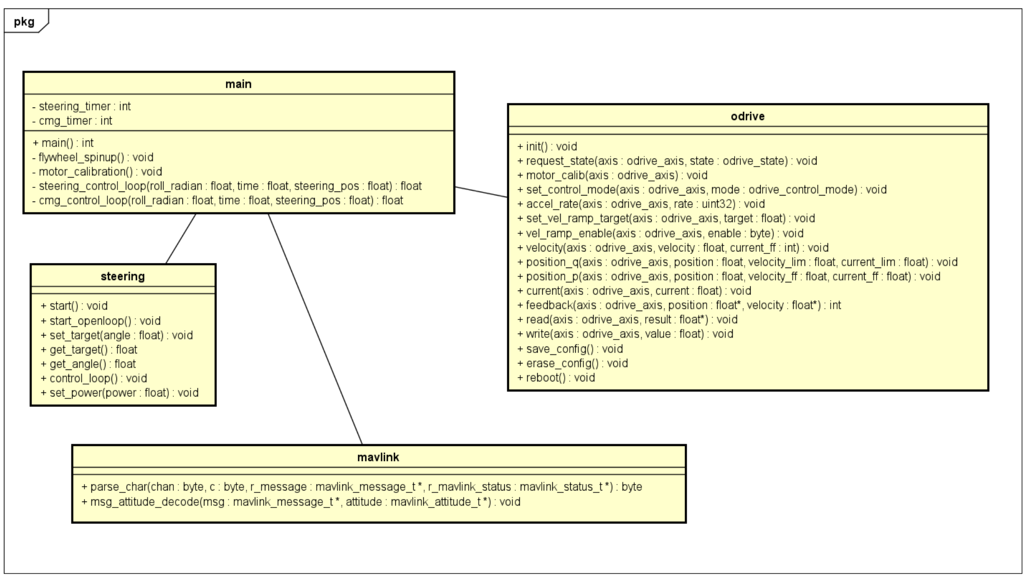

Figure 4.7: Software APIs for external hardware.

Strict timing requirements within the balance controller are maintained through the application of timer triggered events. Event timers are asynchronously decremented by the PSoC hardware during the execution of a continuously running event loop. When a timer reaches zero (expires), the event loop triggers that event and resets the associated timer by adding the timer period back to the timer counter. This approach maintains consistent timing while also preventing starvation, which could occur if events were triggered directly by a timer interrupt. If the timer counter for an event becomes increasingly negative over time, it can be determined that the average event loop iteration duration is longer than the requested period for that event.

For experimental data collection, the microcontroller sends data to a connected PC over a USB UART serial connection. The data can be logged with a custom data logging and visualization application or with a conventional serial terminal, such as PuTTY. This data can then be synchronized with data collected from the motion capture system. The values sent for the experiment described in the next section include: roll angle, roll angular velocity, gimbal angle, gimbal velocity, and the time difference between executions of the balance control loop.

4.4 Controls and Testing

To test the effectiveness of the CMG for stationary balancing, a cascaded PID controller was implemented to keep the bicycle upright while also preventing CMG saturation. The balance controller inputs and outputs are indicated in Figure 4.8.

The torque generated by a CMG is proportional to the gimbal precession rate $\dot{\varphi}_\omega$, and is directed along the cross product of the flywheel and gimbal angular velocities. The flywheel characteristics are shown in Table 4.2, where m is the flywheel mass, I is the moment of inertia about the flywheel axis, ω is the angular velocity used for the experiment, and L is the resulting angular momentum about the flywheel axis.

m	I	ω	L
6.516 kg	0.0313 kg/m^2	456.0 rad/s	14.55 $kg \cdot m^2/s$

Table 4.2: CMG flywheel characteristics.

The outer PID controller minimizes the error between the measured bicycle roll

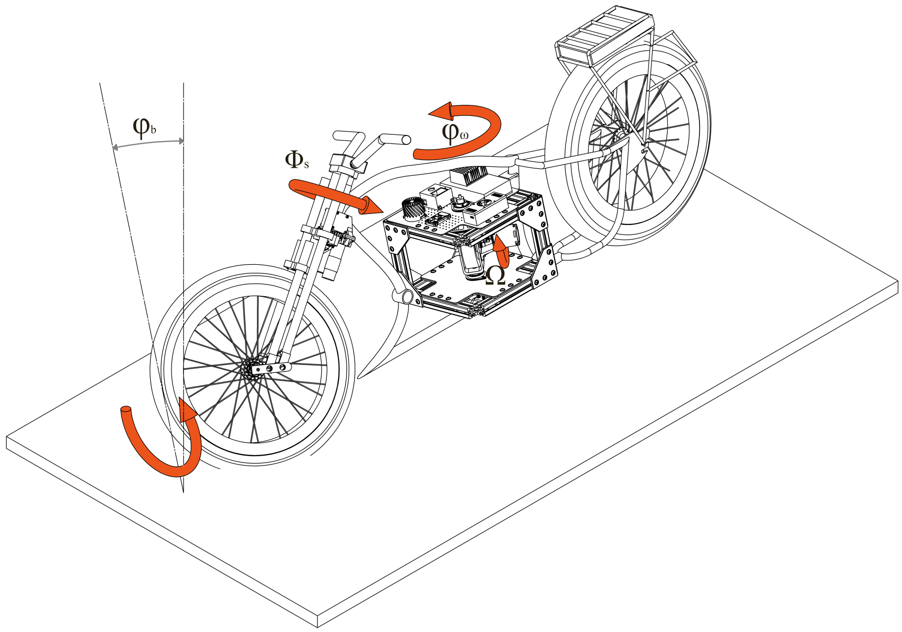

Figure 4.8: Bicycle balance controller input and output parameters.

angle φ_b obtained from the IMU and the roll setpoint, which is 0 (upright) for stationary balancing. Thus, a displacement from the upright position causes the CMG to gimbal to rotate, producing a torque driving the bicycle back to the upright position.

However, using a PID controller for only bicycle roll angle leads to a problem with actuator saturation. Since the CMG torque is normal to the gimbal and flywheel rotation vectors, the component of output torque along the bicycle roll axis goes to zero as the gimbal rotates towards $\pm\pi/2$ from the centered position. For the CMG to balance the bicycle for extended periods, it is also necessary to drive the gimbal back toward the centered position. This is accomplished by cascading the outer PID controller with a second PID controller with CMG position φ_ω as its input. The controller block diagram is shown in Figure 4.9.

Kp	Ki	Kd	eKp	eKi
16.5	0.5	3.76	2.5	4.5

Table 4.3: Control gains used for balance testing.

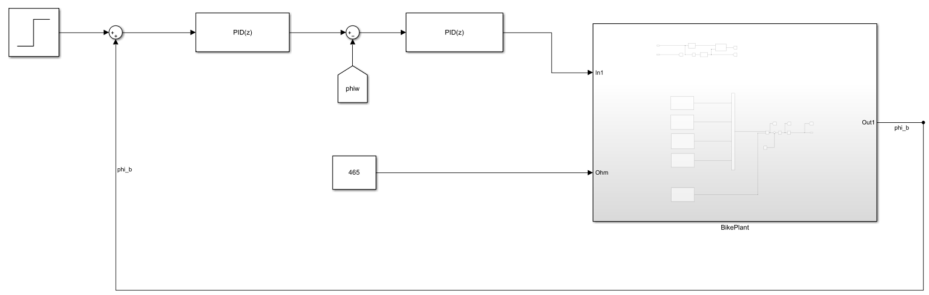

Figure 4.9: Cascaded PID controller in Simulink.

The balancing system was tested three times, successively, within a Vicon motion capture system. This setup enabled capturing the real-world bicycle roll angle along with data from the onboard sensors on the bike, as described in section 4.3.2. The control gains shown in Table 4.3 were used for these tests. The control gains for the outer balance control loop are Kp, Ki, and Kd, and the gains for the inner gimbal control loop are eKp and eKi.

The controller parameters were initialized with parameters used in a Simulink simulation of the bicycle system. The parameters were manually tuned to improve balancing performance. Increasing Ki makes the CMG respond faster to a small error in roll angle. Increasing Kd makes the CMG respond more quickly when the bike starts to fall to the side. However, increasing Kd too much leads to rapid jittering and instability. eKp and eKi determine how quickly the gimbal returns to the centered position to prevent CMG saturation.

Figure 4.10 shows a comparison of the IMU estimated roll angle (blue) and the motion capture measured roll angle (red), for a bicycle balance test. During this test, the bicycle was able to balance for approximately 7.5 seconds before falling. Three balance tests were conducted in this manner. Data from all three trials can be found in Appendix B.

The difference in oscillation magnitude between the motion capture results and the IMU estimate is likely due in part to twisting of the bicycle frame due to the

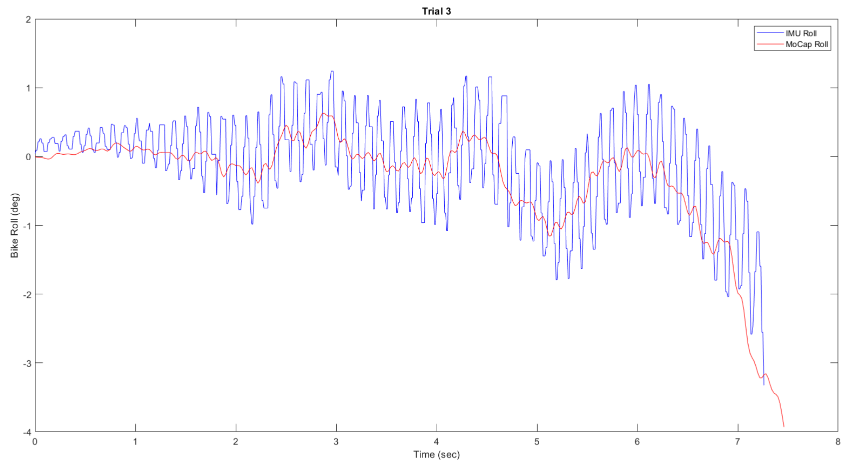

Figure 4.10: Bicycle IMU and motion capture roll for one trial.

CMG torque, but could also be due in part to estimation error within the IMU itself. Possible remedies for this discrepancy would be to adjust the parameters in the IMU filter and to move the IMU and motion capture markers closer together on the bike. Adding additional IMUs in different locations on the bicycle would enable fusing data from multiple sources to obtain a more accurate estimate as well.

In all three tests, the bicycle was able to balance in the upright position for approximately seven to eight seconds before falling due to increasing oscillations. The above-mentioned difference between the actual and IMU roll could be a potential cause of the instability because the controller is not able to obtain the correct value for the roll angle and rate. This causes the controller to overshoot and jitter rapidly. The vibration further contributes to IMU drift, driving the CMG to the saturation point.

It is also possible to improve balancing performance by implementing a different type of controller. Since verifying the actuator capability was the primary objective of these tests, more robust control strategies were not applied due to time constraints.

Chapter 5

DISCUSSION

5.1 Conclusion

Providing balance assistance to a human bicycle rider is a complex task that requires understanding both how to control a bicycle and how to perform this control in the presence of a human rider.

The research question "How can steering intent be identified from human-bicycle interaction forces?" was addressed by the development of a human-bicycle interaction force measurement for non-invasive rider pose estimation. This system expands on my previous work with the force-sensitive bicycle seat. The addition of force sensors to the handlebars and pedals of Bike 1 provides the capability for improved pose estimation over that provided by the seat alone. While this work is similar to that presented in Zhang *et al.* (2013), it does not rely on the use of an IMU or other wearable sensors attached to the rider's body. An outdoor test was conducted to verify the system's functionality, and the results were successfully used to identify relationships between pedal, seat, and handlebar forces. A steering motor is included in the human-bicycle interaction system for creating controlled steering torque disturbances, with the intent of investigating "How do healthy cyclists respond to induced bicycle steering disturbances?" Further motion-capture testing is required to fully answer these research questions.

The research question "How can controllable balance assistance be provided in a self-contained bicycle system" was addressed by the addition of steering and gyroscopic actuators to a purpose-built bicycle frame. The actuators developed in this thesis provide the means to keep the Smart Bike upright under a variety of conditions. The effectiveness of the control moment gyroscope was successfully demonstrated with the implementation of a cascade controller. A computer interface was developed to support manually tuning this controller during operation, which was sufficient to demonstrate the performance of the CMG. The steering actuator provides a compact and energy-efficient mechanism for controlling the bicycle while in motion, and for possibly supplementing the CMG during stationary balancing.

This represents a significant improvement from the systems initially presented in Deng *et al.* (2018) and detailed in Bush (2019), both in terms of actuator capability an overall system design. The size and mass of the large bicycle have made it more difficult to use a CMG for balancing than it was for the small bicycles in presented in Beznos *et al.* (1998) and Lam (2011), but the lower center of mass of Bike 2 decreased the torque requirement from the previous high CMG installation on Bike 1. The design changes also make it easier to perform necessary changes and to conduct tests in a controlled and safe manner.

Ultimately, the Smart Bike is a good research platform for future investigation of controls and human-robot interaction. The design utilizes well-known and accessible technologies that will be easy for researchers to build off of in the future. The system is also designed in modules so that it can be easily upgraded to meet future demands.

5.2 Future Work

Future work will include the integration of the bicycle subsystems to provide balance assistance across the full range of bicycle speeds, with and without a human rider. Completion of the human pose estimation testing procedure within a motion-capture environment will help with validating the effectiveness of the human-bicycle interaction system. Additionally, the data collected from these experiments will be useful for evaluating previously proposed human-bicycle interaction models.

Implementation of robust control for the steering balance system will help the bicycle to balance on uneven ground and in the presence of other disturbances. Improvement of the steering balance controller will also enable controlling the bicycle's trajectory in addition to the roll angle. Trajectory control is essential for autonomous operation and automatic obstacle avoidance. The CMG balance controller will also be improved and integrated into a muti-input multi-output control system with the steering balance control.

The application of autonomous vehicle technology to the Smart Bike is also an area of interest. By enabling autonomous bicycle operation, additional applications in bike-sharing and autonomous delivery are possible. Possible applications also exist in the areas of simultaneous localization and mapping (SLAM) in areas that are not suitable for larger vehicles, studying bicycle-car interaction, and possibly bicycle-unmanned aerial vehicle (UAV) interaction.

Additional areas of interest lie with alternate bicycle configurations and studying the health impacts of bicycling. For example, a recumbent bicycle has a lower center of mass and may be easier to balance automatically. Additionally, recumbent bicycles provide more direct support to the back of the rider and may be more suitable for disabled riders. The human force sensing system may also be useful for studying the impact of seat position and bicycle sizing in relation to rider comfort and safety.

REFERENCES

Álvarez, G. and J. Vinyolas, "A new bicycle pedal design for on-road measurements of cycling forces", Journal of applied biomechanics **12**, 1, 130–142 (1996).

Beznos, A., A. Formal'Sky, E. Gurfinkel, D. Jicharev, A. Lensky, K. Savitsky and L. Tchesalin, "Control of autonomous motion of two-wheel bicycle with gyroscopic stabilisation", in "Proceedings. 1998 IEEE International Conference on Robotics and Automation (Cat. No. 98CH36146)", vol. 3, pp. 2670–2675 (IEEE, 1998).

Bressel, E. and J. Cronin, "Bicycle seat interface pressure: reliability, validity, and influence of hand position and workload", Journal of biomechanics **38**, 6, 1325–1331 (2005).

Bush, J. E., "Automated bicycle human-in-the-loop control", (2019).

Chen, K., Y. Zhang and J. Yi, "An integrated physical-learning model of physical human-robot interactions: A bikebot riding example", in "ASME 2014 Dynamic Systems and Control Conference", pp. V003T42A002–V003T42A002 (American Society of Mechanical Engineers, 2014).

Cherry, C., "Electric bike use in china and their impacts on the environment, safety, mobility and accessibility", (2007).

Cline, D. J., "Bicycle power meter", US Patent 5,031,455 (1991).

Deng, W., S. Moore, J. Bush, M. Mabey and W. Zhang, "Towards automated bicycles: Achieving self-balance using steering control", in "ASME 2018 Dynamic Systems and Control Conference", pp. V002T24A012–V002T24A012 (American Society of Mechanical Engineers, 2018).

Dozza, M. and A. Fernandez, "Understanding bicycle dynamics and cyclist behavior from naturalistic field data (november 2012)", IEEE Transactions on intelligent transportation systems **15**, 1, 376–384 (2013).

Iuchi, K., H. Niki and T. Murakami, "Attitude control of bicycle motion by steering angle and variable cog control", in "31st Annual Conference of IEEE Industrial Electronics Society, 2005. IECON 2005.", pp. 6–pp (IEEE, 2005).

Jones, D. E., "The stability of the bicycle", Physics today **23**, 4, 34–40 (1970).

Keo, L. and M. Yamakita, "Controller design of an autonomous bicycle with both steering and balancer controls", in "2009 IEEE Control Applications,(CCA) & Intelligent Control,(ISIC)", pp. 1294–1299 (IEEE, 2009).

Kim, N. G., C. K. Yoo and J. J. Im, "A new rehabilitation training system for postural balance control using virtual reality technology", IEEE Transactions on Rehabilitation Engineering **7**, 4, 482–485 (1999).

Kooijman, J., A. Schwab and J. K. Moore, “Some observations on human control of a bicycle”, in “ASME 2009 International Design Engineering Technical Conferences and Computers and Information in Engineering Conference”, pp. 2021–2028 (American Society of Mechanical Engineers, 2009).

Lam, P. Y., “Gyroscopic stabilization of a kid-size bicycle”, in “2011 IEEE 5th International Conference on Cybernetics and Intelligent Systems (CIS)”, pp. 247–252 (IEEE, 2011).

Leitner, T., H. Kirchsteiger, H. Trogmann and L. del Re, “Model based control of human heart rate on a bicycle ergometer”, in “2014 European Control Conference (ECC)”, pp. 1516–1521 (IEEE, 2014).

Lindsay, G., A. Macmillan and A. Woodward, “Moving urban trips from cars to bicycles: impact on health and emissions”, Australian and New Zealand journal of public health **35**, 1, 54–60 (2011).

Manufacturing, M., “Murata boy and murata girl”, (2008).

Meyer, D., W. Zhang and M. Tomizuka, “Sliding mode control for heart rate regulation of electric bicycle riders”, in “ASME 2015 Dynamic Systems and Control Conference”, (American Society of Mechanical Engineers Digital Collection, 2015).

Mohammadi-Abdar, H., A. L. Ridgel, F. M. Discenzo and K. A. Loparo, “Design and development of a smart exercise bike for motor rehabilitation in individuals with parkinson’s disease”, IEEE/ASME Transactions on Mechatronics **21**, 3, 1650–1658 (2015).

Stone, C. and M. L. Hull, “Rider/bicycle interaction loads during standing treadmill cycling”, Journal of applied biomechanics **9**, 3, 202–218 (1993).

Timoshenko, S. P. and D. H. Young, “Advanced dynamics”, (1948).

Wang, P., J. Yi, T. Liu and Y. Zhang, “Trajectory tracking and balance control of an autonomous bikebot”, in “2017 IEEE International Conference on Robotics and Automation (ICRA)”, pp. 2414–2419 (IEEE, 2017).

Woodcock, J., M. Tainio, J. Cheshire, O. O’Brien and A. Goodman, “Health effects of the london bicycle sharing system: health impact modelling study”, Bmj **348**, g425 (2014).

Zhang, Y., K. Chen and J. Yi, “Rider trunk and bicycle pose estimation with fusion of force/inertial sensors”, IEEE Transactions on Biomedical engineering **60**, 9, 2541–2551 (2013).

APPENDIX A

LOAD CELL CHARACTERISTICS

Table A.2 shows each load cell and its characteristics, along with the mappings between sensor location and sensor axis. Sensor scaling factors are calculated with equation 3.6 and the global parameters in table A.1.

Property	Value
Excitation	5.0 V
Gain	16
ADC Bits	18
ADC Range	1.024 V

Table A.1: Global load cell parameters.

Sensor Location	Sensor Axis	Model No.	Range (N)	Response (mV/V)	Sign	Scale
Handle Left X	Y	F3G-1kN	1000	1.1795	+	0.082795
Handle Left Y	Z	F3G-1kN	1000	-0.9153	-	-0.10669
Handle Left Z	X	F3G-1kN	1000	1.2035	+	0.081144
Handle Right X	Y	F3G-1kN	1000	1.1583	-	-0.08431
Handle Right Y	Z	F3G-1kN	1000	0.9894	+	0.098702
Handle Right Z	X	F3G-1kN	1000	1.2289	-	-0.07947
Seat Front	N/A	FX1901-0100	444.8	20	-	-0.00217
Seat Left	N/A	FX1901-0100	444.8	20	-	-0.00217
Seat Right	N/A	FX1901-0100	444.8	20	-	-0.00217
Pedal Left	N/A	FCB-B-1kN	1000	1.48	-	-0.06598
Pedal Right	N/A	FCB-B-1kN	1000	1.50	-	-0.06510

Table A.2: Load cell characteristics and scaling factors.

APPENDIX B

BALANCE TEST DATA

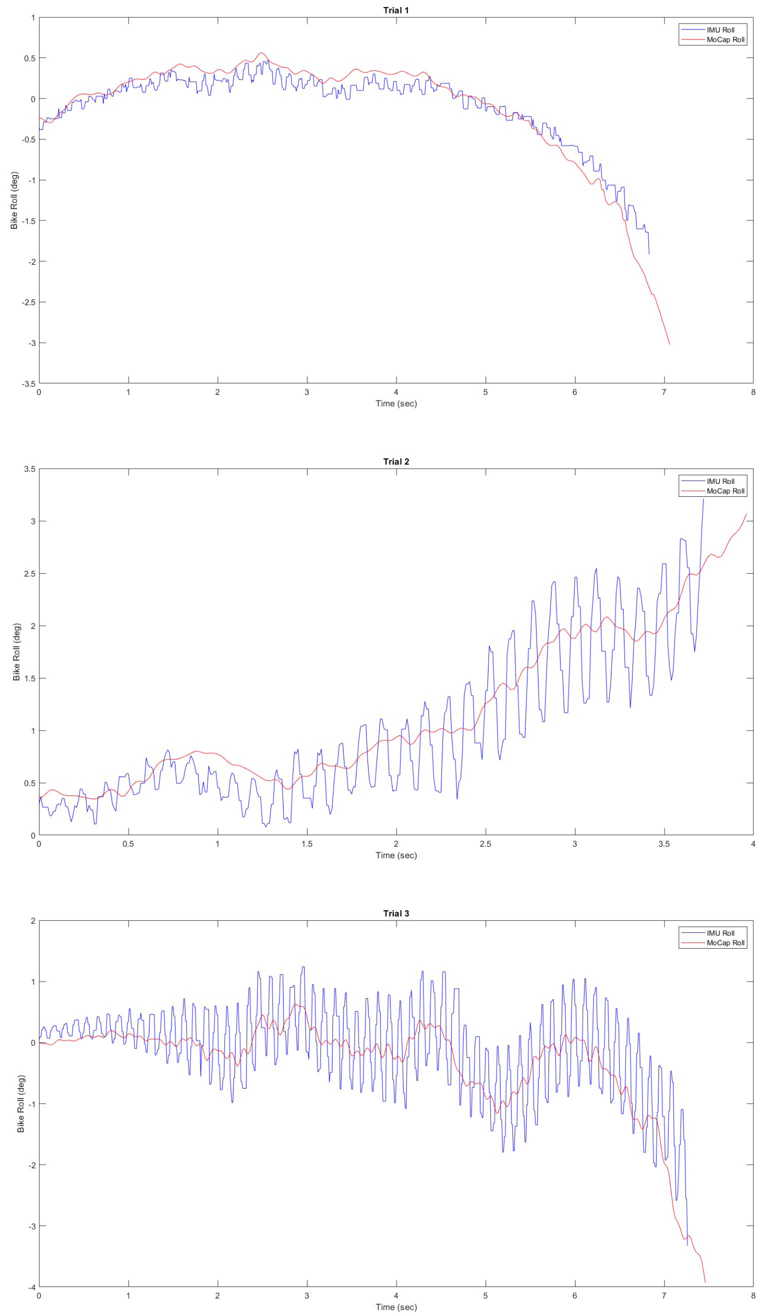

Figure B.1: Motion capture and IMU measured roll for three trials.

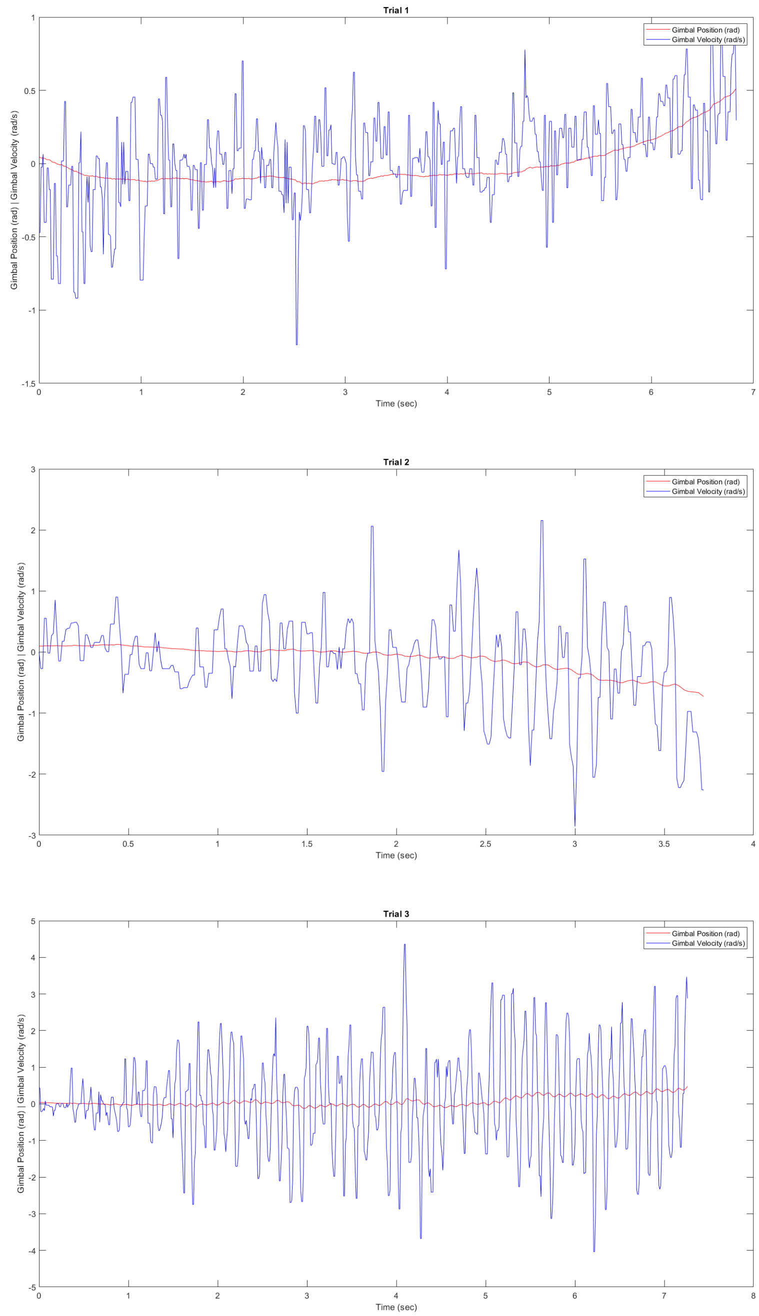

Figure B.2: CMG gimbal position and velocity for three trials.